

Miniaturized Broadband Microwave Permittivity Sensing for Biomedical Applications

Vlachogiannakis, Gerasimos; Hu, Zhebin; Shivamurthy, Harshitha Thippur; Neto, Andrea; Pertijs, Michiel A.P.; De Vreede, Leo C.N.; Spirito, Marco

DOI

[10.1109/JERM.2018.2882564](https://doi.org/10.1109/JERM.2018.2882564)

Publication date

2019

Document Version

Final published version

Published in

IEEE Journal of Electromagnetics, RF and Microwaves in Medicine and Biology

Citation (APA)

Vlachogiannakis, G., Hu, Z., Shivamurthy, H. T., Neto, A., Pertijs, M. A. P., De Vreede, L. C. N., & Spirito, M. (2019). Miniaturized Broadband Microwave Permittivity Sensing for Biomedical Applications. *IEEE Journal of Electromagnetics, RF and Microwaves in Medicine and Biology*, 3(1), 48-55. Article 8542742. <https://doi.org/10.1109/JERM.2018.2882564>

Important note

To cite this publication, please use the final published version (if applicable). Please check the document version above.

Copyright

Other than for strictly personal use, it is not permitted to download, forward or distribute the text or part of it, without the consent of the author(s) and/or copyright holder(s), unless the work is under an open content license such as Creative Commons.

Takedown policy

Please contact us and provide details if you believe this document breaches copyrights. We will remove access to the work immediately and investigate your claim.

Miniaturized Broadband Microwave Permittivity Sensing for Biomedical Applications

Gerasimos Vlachogiannakis , *Student Member, IEEE*, Zhebin Hu,
Harshitha Thippur Shivamurthy, *Student Member, IEEE*, Andrea Neto , *Fellow, IEEE*,
Michiel A. P. Pertijs , *Senior Member, IEEE*, Leo C. N. de Vreede, *Senior Member, IEEE*,
and Marco Spirito, *Member, IEEE*

Abstract—We present a compact, scalable, and broadband architecture for the implementation of complex microwave permittivity sensors in complementary metal-oxide semiconductor (CMOS) technology. The proposed architecture consists of a patch sensor embedded in a programmable balanced readout bridge and performs third and fifth harmonic downconversion for fast multi-frequency readout. Circuits designed can act as the basic building block for a wide span of biomedical applications, ranging from wearables to permittivity imaging. Experimental results of manufactured prototypes demonstrate measurement noise reduction through bridge balancing, Debye model parameter estimation of independent material with a 1.6% error using full frequency dataset, and 5.3% in high energy efficiency mode, as well as image construction based on material permittivity differences.

Index Terms—Bridge circuits, biomedical sensors, complementary metal-oxide semiconductor (CMOS) sensors, complex permittivity measurement, microwave sensors.

I. INTRODUCTION

BROADBAND dielectric spectroscopy is a useful, non-destructive diagnostic tool for the characterization of biological materials. Its applicability derives from the unique frequency-specific dielectric footprint of biological materials which varies in conjunction with their composition or physiological state (e.g., water percentage, mixture concentration, etc). As a result, a large number of potential applications arise, ranging from traditional clinical and point-of-care scenarios to the increasingly emerging area of wearable devices. Examples include in-vivo tissue hydration monitoring, label-free malignant tissue inspection as an assisting tool in removal surgery,

Manuscript received July 29, 2018; revised September 29, 2018 and November 1, 2018; accepted November 8, 2018. Date of publication November 21, 2018; date of current version February 20, 2019. This work was supported by the Dutch Technology Foundation (STW/NWO), Project INFORMER 13010. This paper was presented in part at the IEEE MTT-S International Microwave Biomedical Conference, Philadelphia, PA, Jun. 2018. (*Corresponding author: Gerasimos Vlachogiannakis.*)

G. Vlachogiannakis, H. T. Shivamurthy, A. Neto, M. A. P. Pertijs, L. C. N. de Vreede, and M. Spirito are with the Department of Electrical Engineering, Mathematics and Computer Science, Delft University of Technology, Delft 2628 CD, The Netherlands (e-mail: G.Vlachogiannakis@tudelft.nl; H.Thippur Shivamurthy@tudelft.nl; a.neto@tudelft.nl; M.A.P.Pertijs@tudelft.nl; l.c.n.deVreede@tudelft.nl; M.Spirito@tudelft.nl).

Z. Hu was with Delft University of Technology, Delft 2628 CD, The Netherlands. He is now with HiSilicon Technologies Co., Ltd., Shanghai 200120, China (e-mail: huzhebin.ee@gmail.com).

Digital Object Identifier 10.1109/JERM.2018.2882564

evaluation of drug penetration through skin and blood glucose concentration measurement [1]–[4].

Wide adoption of permittivity sensors in the biomedical domain relies on the ability to manufacture miniaturized yet accurate permittivity sensors. Portability, multi-sensor integration and high energy efficiency are important features in the wearable market, while small sensing area is significant to achieve high spatial resolution in imaging for intra-operative assisting technology. Moreover, operation up to a few GHz will provide field penetration advantages as well as broadband measurement datasets in order to more accurately extract material characteristics, linking to increased specificity and sensitivity of the diagnostic tools. All the above features are achievable through the use of widespread sub- μm complementary metal-oxide semiconductor (CMOS) technology present in an abundance of general-purpose integrated circuits. CMOS also enables co-integration with other medical sensors and with required signal conditioning and digital processing circuits on a single chip.

The following sections elaborate on a compact, multi-purpose permittivity sensor architecture suitable for a wide range of biomedical applications [5]. The proposed approach, briefly presented in [6], comprises a broadband permittivity sensing architecture implemented in CMOS technology that makes use of a fast, multi-harmonic frequency readout and satisfies real-time requirements, while offering low energy consumption. This contribution details on different measurement scenarios that show accuracy, time and energy efficiency improvement when both real and imaginary part of permittivity are acquired. Moreover, an additional fabricated prototype demonstrates for the first time the ability to perform microwave permittivity imaging by including multiple sensors of the proposed architecture within a single chip.

II. CMOS PERMITTIVITY SENSOR IMPLEMENTATION

A. Sensing Element

The sensing element acts as a transducer of the material under test (MUT) complex permittivity ($\epsilon^* = \epsilon' - j\epsilon''$) into an equivalent lumped conductance (G) and capacitance (C)

$$Y_s(\epsilon^*, \omega) = G(\epsilon', \epsilon'', \omega) + j\omega C(\epsilon', \epsilon'', \omega). \quad (1)$$

The mapping relation between the sensor admittance Y_s and permittivity can be provided through either electromagnetic

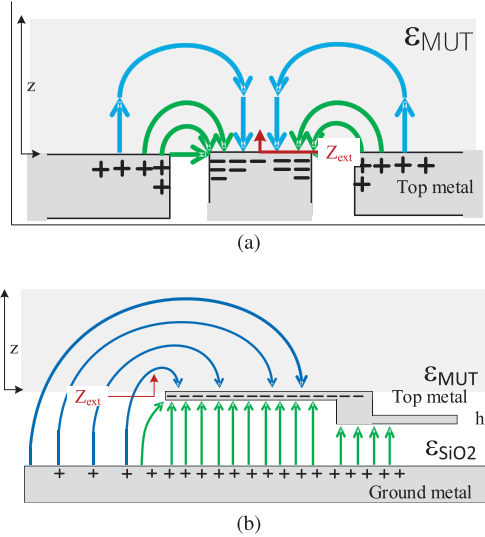


Fig. 1. Cross sections and pictorial representation of field lines and charge distribution for two candidate sensing elements. (a) Differential sensing element. (b) Single-ended patch.

simulations or analytical formulas. In principle, the real and imaginary part of permittivity affect the capacitance and conductance, respectively, although a cross-correlation can still exist, depending on the geometry and the element's self conductance and capacitance.

Based on the geometry, two different sensing element styles are considered: a co-planar structure, either in the form of a transmission line or a co-planar metal-oxide-metal (MoM) capacitor, shown in Fig. 1(a), or a patch sensor, sketched in Fig. 1(b). To accommodate interfacing with a material-under-test (MUT), any geometry needs to be implemented on the top layer of the available CMOS metal stack (FEOL – back-end-of-line). Additionally, a passivation layer opening is required for direct contact, a typical process in CMOS fabrication used for bondpad generation.

Many integrated permittivity sensor implementations utilize a co-planar structure, based on the fact that they can achieve a high sensitivity and provide access for fully-differential readout connection [7]–[12]. We can define the sensitivity of a permittivity sensing element as a relative impedance variation at the sensor–MUT interface Z_{ext} in the presence of MUT versus a reference material ϵ_{ref} (in this case air)

$$S = \frac{Z_{ext}(\epsilon_{ref}) - Z_{ext}(\epsilon_{MUT})}{Z_{ext}(\epsilon_{ref}) + Z_{ext}(\epsilon_{MUT})}. \quad (2)$$

A comparison of element sensitivity for two structures of same footprint ($100 \times 100 \mu\text{m}$) in Fig. 2(a) shows that the co-planar implementation is 60% more sensitive to MUT permittivity variations.

However, the sensitivity definition is confined to the element surface and does not provide information on the penetration depth capabilities. Shown in Fig. 2(b) is the intensity of electric field component, which is normal to the element surface, normalized to the maximum field intensity (present at the interface $-z = 0$). For a patch sensor, a persistence of the field deeper

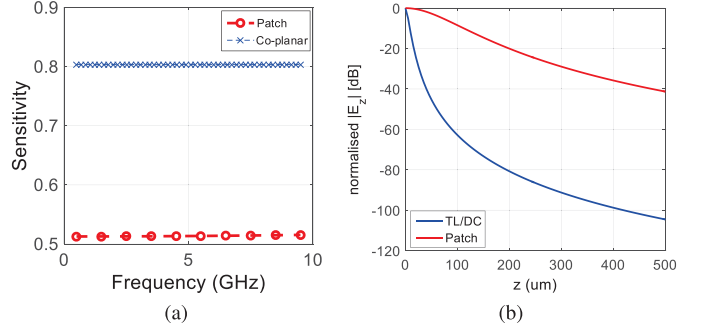


Fig. 2. Comparison of (a) element sensitivity and (b) magnitude of normal electric field component normalized to the field intensity at the element–MUT interface between patch and co-planar capacitive elements.

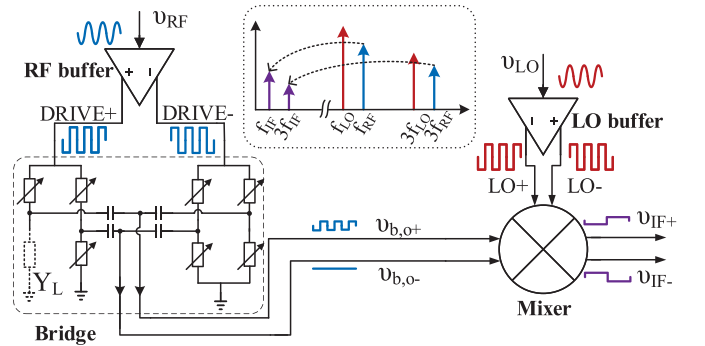


Fig. 3. Core architecture of permittivity sensor readout, featuring reconfigurable double balanced impedance bridge and multiharmonic RF downconversion.

in the MUT is demonstrated compared to the co-planar sensor, due to the distance of the negative/ground plane from the sensor aperture. This characteristic tolerance of the patch sensor to different MUT depths is useful in measurement environments where possible air gaps might be present or permittivity differences at a larger depths need to be resolved. Moreover, single-ended sensing elements allow more flexibility in field line shaping when used in a matrix configuration, i.e., when driving neighboring elements in- or out-of-phase, giving the possibility to reconfigurably generate co-planar sensors of variable size and distance. Based on the above, for the purposes of this work, a single-ended patch is proposed.

B. Readout Architecture

Since the sensing element represents a variable admittance, it can be embedded into an ac-driven Wheatstone bridge (see Fig. 3). By varying the driving frequency of the bridge (DRIVE+, DRIVE–), a voltage of same frequency emerges at the output of the bridge whose amplitude is given by

$$v_{b,o} = (DRIVE) \cdot \frac{Y_L}{4Y_0 + 2Y_L} \quad (3)$$

where $Y_L = G_L + jB_L$ the permittivity-varying admittance, $Y_0 = G_0 + jB_0$ the admittance of other bridge branches, and DRIVE is the amplitude of the bridge excitation signal. It can be analyzed that a bridge in balanced mode, i.e., $Y_L \approx Y_0$ has the largest sensitivity to load variations and is less prone to noise

appearing from the driving buffer [5]. Thus, a programmable admittance Y_0 is used, in the form of a switched capacitance, in order to match the measurement load to the measured permittivity ranges.

Since admittances are complex variables, the output voltage can be broken down into real and imaginary part as well. Analyzing (3) further, we can find a linear relation of the inverse bridge output to the real and imaginary load admittance:

$$\Re \left\{ \frac{1}{\Delta v_{b,o}} \right\} = \frac{1}{v_{in}} (2 + 4G_0 \cdot G_{Lw} + 4B_0 \cdot B_{Lw}) \quad (4)$$

and

$$\Im \left\{ \frac{1}{\Delta v_{b,o}} \right\} = \frac{4}{v_{in}} (B_0 \cdot G_{Lw} - G_0 \cdot B_{Lw}) \quad (5)$$

where $G_{Lw} := G_L/|Y_L|^2$ and $B_{Lw} := B_L/|Y_L|^2$ are defined as the weighted load conductance and susceptance values, respectively. Equations (4) and (5) along with a known relationship between permittivity and sensor admittance, allow to perform a calibration for acquiring both real and imaginary part of permittivity.

Note from the schematic of Fig. 3 that a second identical bridge, with the exception of the sensor load, is driven in an anti-phase manner in order to achieve a differential output signal without common-mode components. A differential output is favorable in an on-chip environment in order to make the readout insensitive to noise coupled from other circuits and the ground/supply variations. Moreover, the output of the driver that excites the bridge is a rectangular waveform in an effort to maximize the useful signal, i.e., amplify the effect of the bridge to load variations.

The impedance bridge that provides the permittivity readout is driven at a GHz-range frequency f_{RF} . The maximum characterization frequency is that of the RF buffer exciting the bridge which is, in turn, dependent of the unity gain frequency f_t of the CMOS process used. Typically, excitation frequencies up to $f_t/20$ have been simulated and measured to be feasible, translated to a fundamental buffer frequency of up to 5 GHz for a 40-nm CMOS process. In order to digitize the bridge reading and perform further processing, as would be the case in a compact multi-sensor system-on-chip (SoC), the bridge output is mixed with a signal of frequency f_{LO} to produce a signal at an intermediate frequency $f_{IF} = f_{RF} - f_{LO}$, at which the implementation of an energy-efficient analog-to-digital converter (ADC) is feasible.

Similarly to the bridge buffer providing a rectangular voltage drive to the bridge, the mixer is also driven by a rectangular, harmonically-rich voltage waveform, in order to maximize the conversion gain [13], [14]. The result of such mixing, as shown in the insert of Fig. 3, is that higher harmonics at the bridge output are also downconverted to higher harmonics of f_{IF} . Even though their amplitude is significantly lower than the fundamental harmonic, it is still possible to acquire useful signal and utilize it in material information extraction, as will be shown in experiments.

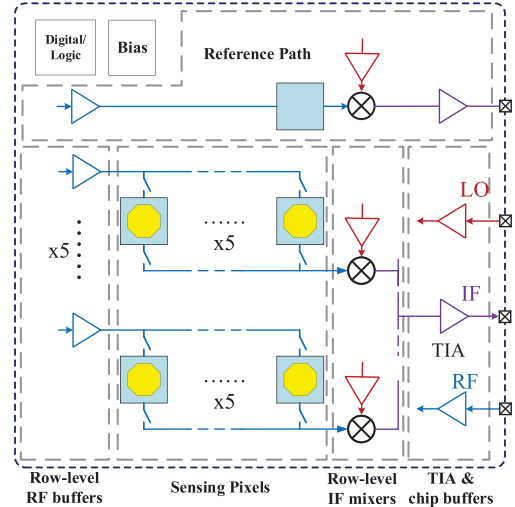


Fig. 4. Block-level schematic of a 5×5 permittivity sensing array.

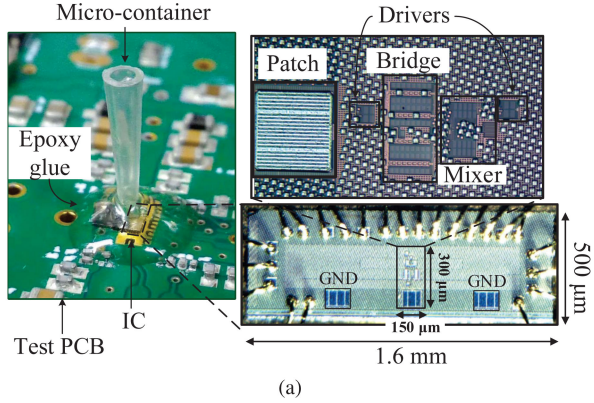
C. Scalable Matrix Concept

The presented architecture can be embedded in array matrix configurations of such microwave permittivity sensors. These can be used for the purpose of imaging or as re-configurable sensing platforms with varying sensing area and relative drive phases between individual pixels and can be applied in applications in which the local differentiation between material is required (e.g., label-free, in-vivo cancer visualization as an assisting tool in removal surgery, and food and flower quality inspection) or cases that require an average permittivity measurement over a large effective area that cannot be covered by a larger patch, due to excessive capacitance. Fig. 4 shows the block diagram of a 5×5 array implementation. Each pixel in the array core comprises a sensing element and its associated bridge with programmable admittance. The output of each pixel is converted to current so that pixel outputs of each row can be connected together and directed to row-level down-conversion mixers. Similarly, row-level buffers distribute the RF driving signal to the pixels. The IF output of the pixels is directed out of the chip where it is digitized. Note that, in an SoC approach, the analog-to-digital converter (ADC) can be placed on-chip.

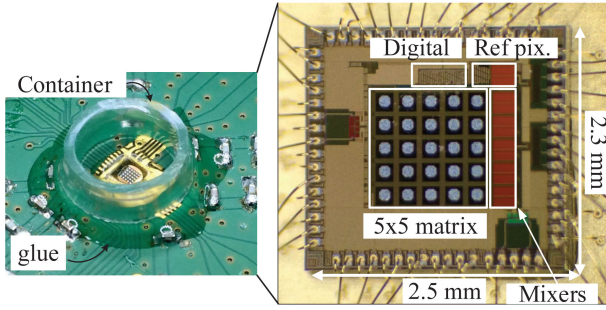
Each pixel drive and readout path can be isolated independently so that a pixel can be read without being driven and vice versa, while a polarity switch in both paths is present that can alternate each pixel drive or readout phase between 0 and 180 degrees. These features can give rise to numerous possibilities in terms of electric field manipulation and allows to trade off among field penetration, direction and spatial resolution.

III. EXPERIMENTAL RESULTS

To evaluate the performance of the proposed microwave permittivity sensing architecture, two demonstrators were designed and fabricated in CMOS technology. Shown in Fig. 5(a) is a 40-nm CMOS implementation of a standalone sensor with a core area of $150 \times 300 \mu\text{m}^2$. The $100 \times 100 \mu\text{m}^2$ patch sensing element is fabricated at the top Al metal of the available CMOS stack and the ground plane is on the bottom metal layer. In



(a)



(b)

Fig. 5. Integrated microwave permittivity sensor implementations in CMOS technology. (a) Standalone sensor in 40-nm technology. (b) 5×5 permittivity sensing array.

Fig. 5(b), a 5×5 array implementation is shown, occupying $2.3 \times 2.5 \mu\text{m}^2$. In this implementation, the sensing element is octagonal with a $100 \mu\text{m}$ edge-to-edge distance and is again implemented on top of the CMOS metal stack. However, the metal ground is chosen to be a higher metal (metal 4) in order for the readout circuits – i.e., buffer, bridge, voltage-to-current conversion and switches – to be laid out beneath the ground plane. The sensor-to-sensor pitch is chosen to be $150 \mu\text{m}$, which is the minimum achievable in order to fit all readout circuits below the patch ground plane. In both implementations, the patches can be in direct contact to the MUT through passivation layer openings. The chips are glued on a PCB with a container on top that allows liquid materials to be interfaced directly to the sensor.

The measurement setup, mainly representative of the standalone sensor, is sketched in Fig. 6. The downconverted output signal of the sensor is amplified and digitized by an external ADC. The harmonic components are then calculated using fast-fourier transform (FFT). To acquire the complex number representation of the output voltage, phase is also acquired along with amplitude, using a reference path. In the standalone chip of Fig. 5(a), the reference path is created by means of an internal MOS switch controlled by a signal lc to disconnect the bridge from the sensing patch and connect it to a fixed load. Two 1-ms measurement intervals are used leaving 0.2 ms in between for transient settling, totaling a 2.2 ms measurement time. In the array implementation, a separate path is implemented on-chip

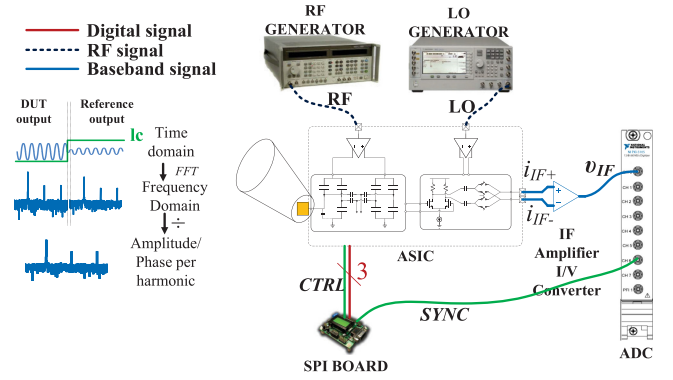


Fig. 6. Permittivity measurement setup of the fabricated ICs and real/imaginary output measurement concept with the use of a reference path measurement.

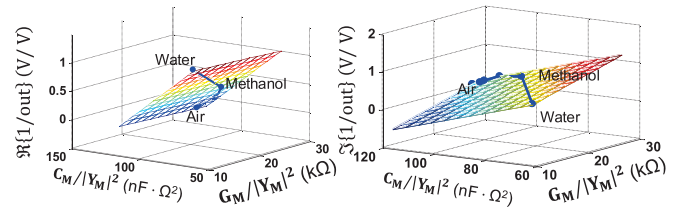


Fig. 7. Calibration surfaces acquired from the measurements of different liquids, showing a linear dependence of the inverse output real and imaginary part to the normalized admittance and conductance.

reducing the measurement time to 1 ms, requiring, however, a second ADC.

To perform absolute measurement of the complex MUT permittivity, a calibration procedure is carried out employing 5 different liquid materials: de-ionized water, methanol, 2-propanol, butanol and air, based on known permittivity values [15]. The relations of (4) and (5) are used to link the inverse output voltage to MUT admittance. Due to the linear form of these equations, the permittivity measurements are located on two surfaces (named as calibration surfaces), for real and imaginary part, respectively, which are found by surface fitting, as shown in Fig. 7. Moreover, the nominal admittance Y_0 is perturbed to find the calibration surface with the least fitting error. This procedure effectively accounts for estimation errors due to process tolerances and modeling mismatches. After acquiring the calibration surfaces, the complex admittance of any measured material is found by solving the inverse surface equations. Last, permittivity is acquired by performing admittance-to-permittivity translation using a rational function model that is obtained from 3D EM simulations of the sensor element, using Keysight EM Pro [16] [17].

All experiments are performed with liquid materials, due to the straightforward interfacing and the knowledge of their permittivity values [15]. In order to advance to semi-rigid material measurements, the proposed hardware has to be augmented with a proper interface to the MUT. This can be achieved by vertical expansion of the patches using solder balls that will allow packaging the chip in plastic and have access to the patches at the same time. Initial investigation during the design procedure has showed that the added capacitance and inductance effect of

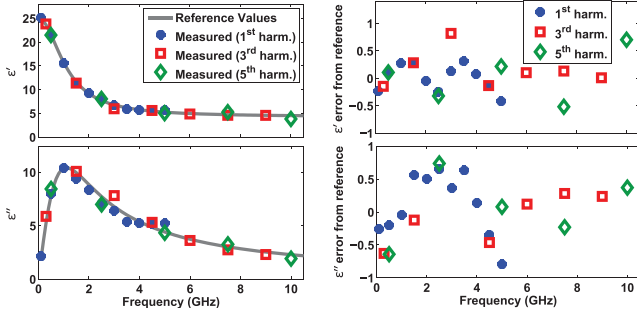


Fig. 8. Independent measurement of ethanol permittivity versus frequency, using first (blue dots) third (red squares), and fifth (green diamonds) harmonics and the associated error from the Debye model. The Debye model of ethanol is shown as a reference value.

these balls is small and has been taken into consideration from the re-configurable bridge capacitance.

A. Permittivity Measurements

Independent permittivity measurements over the sensor frequency range are performed using pure ethanol. The permittivity of ethanol is, for most of the frequency range, located within the sensor calibration range, bounded by air and water. For this experiment, the standalone sensor (see Fig. 5(a)) was utilized and a number of 100 2.2 ms measurements were averaged. The measured complex permittivity values over a frequency range of 0.1–10 GHz are shown in Fig. 8. The fundamental frequency was swept from 0.1 to 5 GHz and a frequency range extension up to 10 GHz was achieved by using the third and fifth harmonics as well. The maximum absolute error compared to the reference values from the debye models is less than 1 for both the real and imaginary part. The third and fifth harmonics did not provide meaningful signal above the fundamental of 3 GHz.

B. Measurement Noise Minimization

As mentioned in Section II-B, the readout bridge admittance is controlled through a set of switched capacitances in order to minimize measurement noise. This effect is demonstrated Fig. 9 where 100 repeated measurements are performed for a totally unbalanced versus a balanced bridge (i.e., bridge admittance closely matches material equivalent admittance) at 1 GHz. It is observed that the real part measurement standard deviation is improved by 70% (0.014 versus 0.054) and the imaginary part by 95% (0.0013 versus 0.034), highlighting the importance of balancing the bridge in order to perform highly repeatable and sensitive measurement. A practical example of this feature in real life scenarios would be to balance the bridge on background tissue before initiating tumor mapping.

C. Debye Model Estimation

To demonstrate the effectiveness of the permittivity sensor in characterizing the MUT and highlight the benefits of a wide measurement bandwidth and complex permittivity readout capability, a nonlinear fitting is performed on the measured data

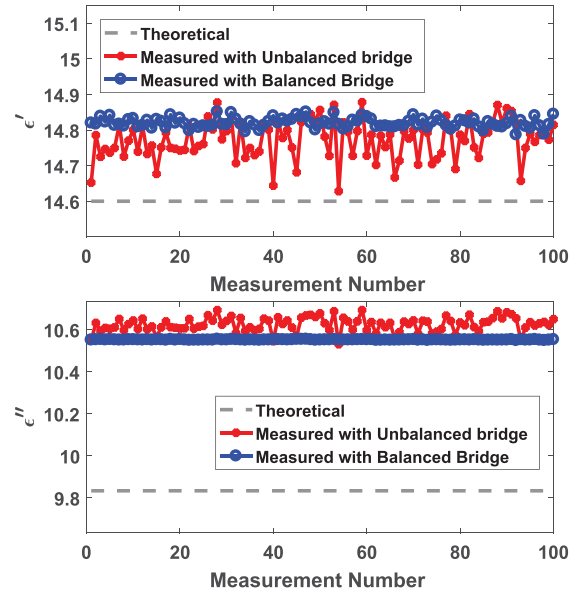


Fig. 9. Repeated measurements of Ethanol at 1 GHz, showing the reduced readout variation for the balanced bridge case (blue trace) versus an imbalanced case (red trace, for both real and imaginary permittivity values).

in order to extract the parameters of ethanol's Debye model

$$\epsilon = \epsilon' - i\epsilon'' = \epsilon_0 + \frac{\epsilon_\infty - \epsilon_0}{1 + (i\lambda f/c)} \quad (6)$$

where ϵ_∞ , ϵ_0 , and λ are the Debye model parameters; f the measurement frequency; and c the speed of light in vacuum [15].

Table I presents the estimated parameters and the related estimation error in a number of test cases. Fundamental frequency varies from 0.1 GHz to 5 GHz with 0.5 GHz step between 0.5 GHz and 5 GHz (11 points in total). All measurements are performed at a speed of 2.2 ms per measurement, producing three frequency points for fundamental frequencies below 2 GHz and two frequency points below 3 GHz. The measured power consumption of the chip is between 1.2 mW at 0.1 GHz and 24 mW at 5 GHz, owing to the hard-clipping multi-harmonic design of the RF and LO buffers that increase power consumption linearly with frequency. Combining the consumption information with the measurement time for each scenario, the energy per measurement can be calculated. It can be seen that using the full frequency range and only real part of permittivity (case 1) provides the least possible error of estimated parameters, even significantly lower than using both real and imaginary part of permittivity for estimation (case 2). This observation could mistakenly lead to the conclusion that imaginary part estimation is more erroneous and even unnecessary, given the fact that a material can be only estimated from ϵ' , and that ϵ'' can be extracted therefrom [18]. The same trend holds when using only the first harmonic, thus a reduced frequency dataset, although the error difference between cases 3 and 4 of Table I is not very significant. Moreover, it is clear that using third and fifth harmonics leads to improved estimation for the same measurement time and energy (cases 1 versus 3).

TABLE I
COMPARISON OF DEBYE MODEL PARAMETER ESTIMATION ACCURACY FOR DIFFERENT SENSOR MEASUREMENT CASES

Measurement case		ϵ_0	ϵ_0 error	ϵ_∞	ϵ_∞ error	λ	λ error	Meas. time	Meas. energy
1	Full frequency dataset, only ϵ'	4.2179	0.99%	25.2227	0.61%	0.2745	1.6%	24.2 ms	13.9 aJ
2	Full frequency dataset, both ϵ' and ϵ''	4.3613	1.32%	25.251	0.72%	0.2829	4.7%		
3	First harmonic, only ϵ'	4.4775	5.1%	25.2827	0.63%	0.2823	4.48%		
4	First harmonic, both ϵ' and ϵ''	4.5193	6.09%	25.211	0.56%	0.2827	4.62%	2.2 ms	0.55 aJ
5	Single meas. (1,3,5 GHz), only ϵ'	4.4888	5.4%	63.9	154.88%	0.6293	132.9%		
6	Single meas. (1,3,5 GHz), both ϵ' and ϵ''	4.0368	5.24%	24.918	0.61%	0.2814	4.15%		

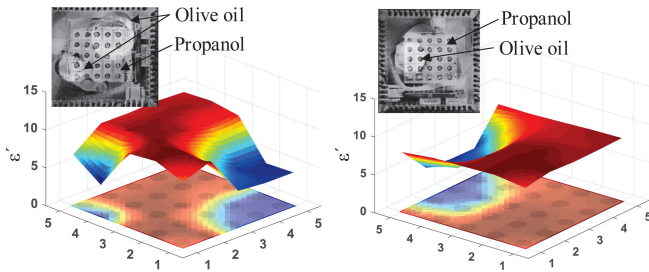


Fig. 10. Three-dimensional permittivity plots and projected images captured by the sensor array chip using drops of olive oil in a base liquid consisting of 2-propanol.

However, in contrast to when using a quite complete frequency dataset, the importance of using both ϵ' and ϵ'' for material estimation, rather than only the former, is becoming significant in a scenario requiring fast or ultra low energy read-out (e.g., in real-time 2-D scanning or wearables). In such a case, only one single harmonic measurement can be acquired at 1 GHz, resulting in indirect acquisition of permittivity on three frequency points (1, 3 and 5 GHz). Using only ϵ' effectively fails to estimate the material characteristics (errors more than 100% observed in case 5), while also utilizing the information of ϵ'' brings the accuracy to much more acceptable levels, highlighting the practical importance of complex permittivity sensing architectures in real-life biomedical devices.

D. Permittivity Imaging

The 5×5 array demonstrator of Fig. 5(b) was calibrated identically to the standalone one and was used to perform 2-D permittivity imaging by sequentially reading out all sensing elements. An inhomogeneous material mix was created by depositing drops of olive oil inside a 2-propanol base, corresponding to a ϵ' contrast of 7.4 to 3 at 900 MHz. The array sensor consumes 153 mW during scanning, when two sensor paths are operating (measurement and reference sensor). The higher power consumption compared to the 40-nm single chip sensor (76.5 mW/pixel versus 6 mW/pixel) is due to the higher supply voltage of 1.8 V and the slower technology node of 130 nm that requires significant increase of RF driving buffers for feeding the array. Fig. 10 shows the ϵ' imaging result for two separate images compared to their optical image. The scan rate corresponds to four images per second and demonstrates a clear contrast permittivity detection function.

TABLE II
SUMMARY OF STATE-OF-THE-ART CMOS INTEGRATED MICROWAVE PERMITTIVITY SENSORS

	[7]	[8]	[9]	[10]	This
Tech. [nm]	350	180	90	180	40 & 130
Freq. range [GHz]	0.05–3	0.62–10	10	0.7–6	0.1–10
Meas. quantity	ϵ'	ϵ', ϵ''	ϵ', ϵ''	ϵ', ϵ''	ϵ', ϵ''
Meas. accuracy	1%	1%	1.5%	3.7%	1.6%
Meas. Energy @ freq	0.77 aJ 1 GHz	59 aJ 1 GHz	N/A	5900 aJ 1 GHz	0.18 aJ 1 GHz
Core area [mm ²]	2.25	2.1	0.81	1.17	0.045
On-chip sensor	No	Yes	Yes	Yes	Yes
Array integration	No	No	No	No	Yes

IV. CONCLUSION

An architecture for complex broadband permittivity sensing was presented. The architecture is compact and energy efficient making it suitable for biomedical applications requiring real-time fast measurements or imaging. Two prototypes were manufactured, demonstrating liquid permittivity measurement, frequency-domain permittivity footprint extraction through Debye model parameter estimation and permittivity imaging.

As summarized in Table II, compared to state-of-the-art CMOS permittivity implementations, the proposed sensor occupies the smallest core area at the highest energy efficiency per single-frequency measurement [7]–[10]. Moreover, it achieves a wideband permittivity measurement and measures both real and imaginary part with highlighted advantages over spotted-frequency counterparts and implementations, measuring only the real part [9], [11], [12]. Finally, this is the first known permittivity sensor topology at RF frequencies to be integrated in a matrix array and demonstrate imaging.

ACKNOWLEDGMENT

The authors would like to thank the RF Department of HiSilicon and NXP for IC fabrication, R. Quan for manufacturing process support, W. Straver and A. Kaichouhi for chip packaging support, and R. Roovers and S. Drago for their contribution in technical discussions.

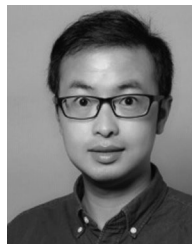
REFERENCES

- [1] P. Mehta, K. Chand, D. Narayanswamy, D. G. Beetner, R. Zoughi, and W. V. Stoecker, "Microwave reflectometry as a novel diagnostic tool for detection of skin cancers," *IEEE Trans. Instrum. Meas.*, vol. 55, no. 4, pp. 1309–1316, Aug. 2006.
- [2] A. P. O'Rourke *et al.*, "Dielectric properties of human normal, malignant and cirrhotic liver tissue: In vivo and ex vivo measurements from 0.5 to 20 GHz using a precision open-ended coaxial probe," *Phys. Med. Biol.*, vol. 52, no. 15, pp. 4707–4719, 2007.
- [3] J. L. Schepps and K. R. Foster, "The UHF and microwave dielectric properties of normal and tumour tissues: Variation in dielectric properties with tissue water content," *Phys. Med. Biol.*, vol. 25, no. 6, pp. 1149–1159, 1980.
- [4] E. Topsakal, T. Karacolak, and E. C. Moreland, "Glucose-dependent dielectric properties of blood plasma," in *Proc. 30th URSI Gen. Assem. Sci. Symp.*, Aug. 2011, pp. 1–4.
- [5] G. Vlachogiannakis, M. A. Pertjjs, M. Spirito, and L. C. de Vreede, "A 40-nm CMOS complex permittivity sensing pixel for material characterization at microwave frequencies," *IEEE Trans. Microw. Theory Tech.*, vol. 66, no. 3, pp. 1619–1634, Mar. 2018.
- [6] G. Vlachogiannakis *et al.*, "A compact energy efficient CMOS permittivity sensor based on multiharmonic downconversion and tunable impedance bridge," in *Proc. IEEE Int. Microw. Biomed. Conf.*, Jun. 2018, pp. 1–3.
- [7] M. Bakhshiani, M. A. Suster, and P. Mohseni, "A broadband sensor interface IC for miniaturized dielectric spectroscopy from MHz to GHz," *IEEE J. Solid-State Circuits*, vol. 49, no. 8, pp. 1669–1681, Aug. 2014.
- [8] M. M. Bajestan, A. A. Helmy, H. Hedayati, and K. Entesari, "A 0.62–10 GHz complex dielectric spectroscopy system in CMOS," *IEEE Trans. Microw. Theory Tech.*, vol. 62, no. 12, pp. 3522–3537, Dec. 2014.
- [9] O. Elhadidy, M. Elkholly, A. A. Helmy, S. Palermo, and K. Entesari, "A CMOS fractional-PLL-based microwave chemical sensor with 1.5% permittivity accuracy," *IEEE Trans. Microw. Theory Tech.*, vol. 61, no. 9, pp. 3402–3416, Sep. 2013.
- [10] O. Elhadidy, S. Shakib, K. Krenek, S. Palermo, and K. Entesari, "A wideband fully-integrated CMOS ring-oscillator PLL-based complex dielectric spectroscopy system," *IEEE Trans. Circuits Syst. I*, vol. 62, no. 8, pp. 1940–1949, Aug. 2015.
- [11] A. A. Helmy *et al.*, "A self-sustained CMOS microwave chemical sensor using a frequency synthesizer," *IEEE J. Solid-State Circuits*, vol. 47, no. 10, pp. 2467–2483, Oct. 2012.
- [12] J.-C. Chien and A. M. Niknejad, "Oscillator-based reactance sensors with injection locking for high-throughput flow cytometry using microwave dielectric spectroscopy," *IEEE J. Solid-State Circuits*, vol. 51, no. 2, pp. 457–472, Feb. 2016.
- [13] R. Bagheri *et al.*, "An 800-MHz–6-GHz software-defined wireless receiver in 90-nm CMOS," *IEEE J. Solid-State Circuits*, vol. 41, no. 12, pp. 2860–2876, Dec. 2006.
- [14] B. Razavi, *RF Microelectronics*. New York, NY, USA: Pearson Education, 2013.
- [15] F. Buckley and A. A. Maryott, "Tables of dielectric dispersion data for pure liquids and dilute solutions," U.S. Dept. Commerce, Nat. Bureau Stand., Gaithersburg, MD, USA, *Tech. Rep.*, 1958, vol. 589.
- [16] J. Anderson, C. Sibbald, and S. Stuchly, "Dielectric measurements using a rational function model," *IEEE Trans. Microw. Theory Tech.*, vol. 42, no. 2, pp. 199–204, Feb. 1994.
- [17] G. Vlachogiannakis, M. Spirito, M. A. P. Pertjjs, and L. C. N. de Vreede, "A 40-nm CMOS permittivity sensor for chemical/biological material characterization at RF/microwave frequencies," in *Proc. IEEE MTT-S Int. Microw. Symp.*, 2016, pp. 1–4.
- [18] C. Kittel, *Elementary Statistical Physics*. Chelmsford, MA, USA: Courier, 2004.



design for biomedical applications and communication.

Gerasimos Vlachogiannakis (S'10) received the diploma in electrical and computer engineering from the National Technical University of Athens, Athens, Greece, in 2011 and the M.Sc. degree (*cum laude*) in microelectronics from the Delft University of Technology (TU), Delft, The Netherlands, where he is currently working toward the Ph.D. degree. As a researcher with TU Delft, he has been involved in the design of RF frequency synthesizers, RF building blocks, and sensors for biomedical purposes. His current research interests include analog and RF circuit



China, as a RF design Engineer. His current research interests are mainly on power amplifiers in integrated circuits.

Zhebin Hu received the B.Sc. degree in electronic and information engineering from the Xiangtan University, Xiangtan, China, in 2009 and the Ph.D. degree in circuits and systems from the University of Electronic Science and Technology of China, Chengdu, China, in 2016. From 2013 to 2015, he was a joint Ph.D. student with the Electronics Research Laboratory, Delft University of Technology, Delft, The Netherlands, where he worked as Postdoctoral Researcher from 2016 to 2018. He is currently working with HiSilicon Technologies Co., Ltd., Shanghai,

photograph and biography not available at the time of publication.



Harshitha Thippur Shivamurthy, photograph and biography not available at the time of publication.

Andrea Neto (M'00–SM'10–F'16) received the Laurea degree (*summa cum laude*) in electronic engineering from the University of Florence, Florence, Italy, in 1994 and the Ph.D. degree in electromagnetics from the University of Siena, Siena, Italy, in 2000. Part of his Ph.D. degree was developed at the European Space Agency Research and Technology Center Noordwijk, The Netherlands. He worked for the Antenna Section with the European Space Agency Research and Technology Center for more than two years. From 2000 to 2001, he was a Postdoctoral Researcher with the California Institute of Technology, Pasadena, CA, USA, where he worked with the Sub-mm Wave Advanced Technology Group. From 2002 to January 2010, he was a Senior Antenna Scientist with TNO Defence, Security, and Safety, The Hague, The Netherlands. In February 2010, he became a Full Professor of applied electromagnetism with the Electrical Engineering, Mathematics and Computer Science Department, Technical University of Delft, Delft, The Netherlands, where he formed and leads the THz Sensing Group. His research interests include the analysis and design of antennas with an emphasis on arrays, dielectric lens antennas, wideband antennas, EBG structures, and THz antennas. He was an Associate Editor for the IEEE TRANSACTIONS ON ANTENNAS AND PROPAGATION (2008–2013) and the IEEE ANTENNAS AND WIRELESS PROPAGATION LETTERS (2005–2013). He is currently an Associate Editor for the IEEE TRANSACTIONS ON THZ SCIENCE AND TECHNOLOGY. He is a member of the Technical Board of the European School of Antennas and organizer of the course on antenna imaging techniques. In 2011, he was the recipient of the European Research Council Starting Grant to perform research on Advanced Antenna Architectures for THz Sensing Systems.



Michiel A. P. Pertjjs (S'99–M'06–SM'10) received the M.Sc. and Ph.D. degrees in electrical engineering (both *cum laude*) from the Delft University of Technology, Delft, The Netherlands, in 2000 and 2005, respectively. From 2005 to 2008, he was with National Semiconductor, Delft, where he designed precision operational amplifiers and instrumentation amplifiers. From 2008 to 2009, he was a Senior Researcher with imec/Holst Centre, Eindhoven, The Netherlands. In 2009, he joined the Electronic Instrumentation Laboratory, Delft University of Technology, where he is now an Associate Professor. He heads a research group focusing on integrated circuits for medical ultrasound and energy-efficient smart sensors. He has authored or co-authored two books, three book chapters, 13 patents, and more than 100 technical papers. He was an Associate Editor for the IEEE JOURNAL OF SOLID-STATE CIRCUITS (JSSC). He is a member of the technical program committee the European Solid-State Circuits Conference and served on the program committees of the International Solid-State Circuits Conference (ISSCC) and the IEEE Sensors Conference. He was the recipient of the ISSCC 2005 Jack Kilby Award for Outstanding Student Paper and the JSSC 2005 Best Paper Award. For his Ph.D. research on high-accuracy CMOS smart temperature sensors, he was the recipient of the 2006 Simon Stevin Gezel Award from the Dutch Technology Foundation STW. In 2014, he was elected the Best Teacher of the EE program at Delft University of Technology.



Leo C. N. de Vreede (M'01–SM'04) received the Ph.D. degree (*cum laude*) from the Delft University of Technology, Delft, The Netherlands, in 1996. In 1996, he was appointed as an Assistant Professor with the Delft University of Technology, working on the nonlinear distortion behavior of bipolar transistors with the Delft Institute of Microelectronics and Submicron Technology. In 1999 and 2015, he was appointed, respectively, Associate and a Full Professor with the Delft University of Technology, where he became responsible for the Electronic Research

Laboratory. During that period, he worked on solutions for improved linearity and RF performance at the device, circuit, and system level. He has co-authored more than 110 IEEE refereed conference and journal papers and holds several patents. His current interest includes RF transmitters, measurement systems, and concepts for wireless circuits and systems. He is co-founder/advisor of Anteverta-mw: a company specializing in RF device characterization. He co-received the IEEE Microwave prize in 2008, was a mentor of the Else Kooi prize awarded Ph.D. work in 2010, and a mentor of the Dow Energy dissertation prize awarded Ph.D. work in 2011. He was received the TUD entrepreneurial scientist Award in 2015. He co-guided several students that won Best Paper Awards at the Bipolar/BiCMOS Circuits and Technology Meeting, PRORISC, GAAS, ESSDERC, IMS, RFIT, and RFIC.



Marco Spirito (S'01–M'08) received the M.Sc. degree (*cum laude*) in electrical engineering from the University of Naples Federico II, Naples, Italy, in 2000 and the Ph.D. degree from the Delft University of Technology, Delft, The Netherlands, in 2006. From 2000 to 2001, he was a Guest Researcher with Infineon Technologies, Munich, Germany. In 2006, he joined the Department of Electronics and Telecommunications Engineering, University of Naples Federico II. In April 2008, he joined the Electronics Research Laboratory, Delft University of Technology,

as an Assistant Professor, where he has been an Associate Professor since April 2013. In 2010 and 2017, he was one of the co-founders of Anteverta-MW and Vertigo Technologies, respectively, which are two companies pioneering innovative measurement instrumentations. His research interests include the development of advanced passive components and building blocks operating in the millimeter and sub-millimeter frequency ranges, the development of characterization setups and calibration techniques for millimeter and sub-millimeter waves, and the design and integration of mmWave sensing systems. He was the recipient of the Best Student Paper Award for his contribution to the 2002 IEEE Bipolar/BiCMOS Circuits and Technology Meeting and the IEEE MTT Society Microwave Prize in 2008. He was the co-recipient of the Best Student Paper Award at IEEE Radio Frequency Integrated Circuits in 2011 and the German Association for American Studies Student Fellowship in 2012.